www.elsevier.com/locate/jmbbm

Load-Bearing in Cortical Bone Microstructure: Selective Stiffening and Heterogeneous Strain Distribution at the Lamellar Level

Orestis L. Katsamenis, Harold M.H. Chong, Orestis G. Andriotis, Philipp J. Thurner

PII: S1751-6161(12)00229-9
DOI: http://dx.doi.org/10.1016/j.jmbbm.2012.08.016
Reference: JMBBM668

To appear in: *Journal of the Mechanical Behavior of Biomedical Materials*

Received date: 18 May 2012
Revised date: 20 August 2012
Accepted date: 21 August 2012

Cite this article as: Orestis L. Katsamenis, Harold M.H. Chong, Orestis G. Andriotis and Philipp J. Thurner, Load-Bearing in Cortical Bone Microstructure: Selective Stiffening and Heterogeneous Strain Distribution at the Lamellar Level, *Journal of the Mechanical Behavior of Biomedical Materials,* http://dx.doi.org/10.1016/j.jmbbm.2012.08.016

Load-Bearing in Cortical Bone Microstructure: Selective Stiffening and Heterogeneous Strain Distribution at the Lamellar Level

Orestis L. Katsamenis[a], Harold M. H. Chong[b], Orestis G. Andriotis[a], Philipp J. Thurner[a]*

[a]Bioengineering Sciences Research Group, Faculty of Engineering and the Environment, University of Southampton, SO17 1BJ, Southampton, UK

[b]School of Electronics and Computer Sciences, University of Southampton, SO17 1BJ, Southampton, UK

*Corresponding author at: University of Southampton, School of Engineering Sciences, Bioengineering Sciences Research Group, Highfield, Southampton SO17 1BJ, United Kingdom. Tel.: +44 238 059 4640.

Email: p.thurner@soton.ac.uk

5/18/2012; 8/20/2012; 8/21/2012

Abstract

An improved understanding of bone mechanics is vital in the development of evaluation strategies for patients at risk of bone fracture. The current evaluation approach based on bone mineral density (BMD) measurements lacks sensitivity, and it has become clear that as well as bone mass, bone quality should also be evaluated. The latter includes, among other parameters, the bone matrix material properties, which in turn depend on the hierarchical structural features that make up bone as well as their composition. Optimal load transfer, energy dissipation and toughening mechanisms have, to some extent, been uncovered in bone. Yet, the origin of these properties and their dependence upon the hierarchical structure and composition of bone are largely unknown. Here we investigate load transfer in the osteonal and sub-osteonal levels and the mechanical behaviour of osteonal lamellae and interlamellar areas during loading. Using cantilever-based nanoindentation, *in situ* microtensile testing during atomic force microscopy (AFM) and digital image correlation (DIC), we report evidence for a previously unknown mechanism. This mechanism transfers load and movement in a manner analogous to the engineered "elastomeric bearing pads" used in large engineering structures. μ-RAMAN microscopy investigations

showed compositional differences between lamellae and interlamellar areas. The latter have lower collagen content but an increased concentration of noncollagenous proteins (NCPs). Hence, NCPs enriched areas on the microscale might be similarly important for bone failure as on the nanoscale. Finally, we managed to capture stable crack propagation within the interlamellar areas in a time-lapsed fashion, proving their significant contribution towards fracture toughness.

Keywords

Cortical bone; Crack propagation; Nanoindentation; Raman spectroscopy; Bone structure

1. Introduction

Bone is a complex nanocomposite material and in its healthy state provides high stiffness and toughness. Age and/or disease related changes in bone lead to over 200,000 fractures in the UK every year. In addition to the significant reduced quality of life for these patients, this also results in an estimated cost of approximately £1.7 bn (Bukhari, 2009) for the National Health Service (NHS); the equivalent cost in the USA is estimated between $5 - $10 bn (~1.5 million fractures) (Riggs and Melton, 1995). Doubling of these costs is soon to be expected in the western world due to aging and increased lifespan of the population (Bukhari, 2009). The main problem faced today is the lack of a reliable fracture risk diagnosis for the individual patient. In clinical practice, the gold standard to predict bone fracture risk is largely based on bone mineral density (BMD) measurements, i.e. bone mass. However, this often fails to accurately predict fracture risk for the individual, as information about bone quality is missing.

Bone is a hierarchical composite material composed of mineralized type I collagen fibrils immersed into a matrix of noncollagenous proteins (NCPs) (Braidotti et al., 2000b; Braidotti et al., 1997b). Several studies on the structure-function relationships of bone on different hierarchical levels, show that age- and disease-related increased fragility cannot be solely attributed to bone mass loss (Hui et al., 1988; Kanis et al., 2005). In addition to bone mass, factors such as age (Hui et al., 1988; Zioupos and Currey, 1998), disease (Cowin, 2001), and genetic background (Jepsen et al., 2001), affect the fragility of bone, independently of bone mass (Hui et al., 1988; Kanis et al.,

2005). This further supports that the extraordinary "material" properties of bone, such as the optimized load transfer and advanced energy dissipation mechanisms (Fantner et al., 2005; Gupta et al., 2006b; Kavukcuoglu et al., 2007), are to be attributed to bone quality.

The term "bone quality" essentially includes all parameters and properties, including (but not limited to) bone mass or BMD, which influence bone mechanical and fracture behaviour (Felsenberg and Boonen, 2005; Ulrich et al., 1997b). For more than twenty years, research on bone quality has been conducted to elucidate specific parameters and the way each one of them affects bone fragility. Since the early 1980s, variations of the degree of mineralization in bones have linked with different mechanical properties of the tissue (Currey, 1984), while almost at the same period, attention was drawn on the importance of collagen maturation and orientation on these properties (Eyre et al., 1988; Viguet-Carrin et al., 2006). With the advent of micro-computed tomography (μCT) it has become clear that the microarchitecture of trabecular bone is also important for bone quality (Fratzl et al., 2004; Ulrich et al., 1997a). Beyond these particular findings it has become clear that there is an overarching hierarchical structure – function relationship, which is perhaps the "holy grail" in understanding the origin of the "material" properties of bone (Weiner et al., 1999; Weiner and Wagner, 1998). Yet, the hierarchical structure – function relationship and their relevance for bone fracture toughness is still not very well understood. The complexity encountered is due to the fact that the final mechanical properties of bone derive from both the individual properties of the different hierarchical components and the way these components interact with each other (Nyman et al., 2005; Rho et al., 1998; Weiner and Wagner, 1998).

Recent computational studies took an important step towards dealing with this fundamental question by incorporating different hierarchical components to their models. Hamed et al., using a bottom-up approach of four different hierarchical levels, with the output of a lower level serving as the input for the modelling of the higher one, were able to predict the effective elastic moduli of cortical bone (Hamed et al., 2010). More recently, Vaughan et al. using a three-scale finite element model, studied the effect of mineral volume fraction, mineral aspect ratio and lamellar orientation on the elastic properties of cortical and trabecular bone (Vaughan et al., 2012). These studies clearly show that changes and/or mechanisms occurring in one

level can have an apparent effect at the properties of the other, and consequently to the overall behaviour of the bone tissue.

Interfaces on various hierarchical levels appear to have important contributions, especially towards fracture toughness, but the exact mechanisms by which they contribute along with their structure and composition have not yet been elucidated in full. A key challenge, formulated by Rho et al. [12], that requires answering is: "…*the lack of knowledge of the properties of the individual constituents [of cortical bone] and their associations in the matrix. What is the nature of the interfaces between the constituents of bone at all length scales?*"

On the nanoscale, the arrangement of basic elements of collagen type I and biological apatite nanocrystals (LeGeros, 1981) into mineralized collagen fibrils, and further into progressively larger structural features is steered by NCPs (Roach, 1994). The result of this complex arrangement on the microscale are the lamellae, which are essentially the micro-building block of mature compact bone (Rho et al., 1998). Each lamella can be described as a hierarchical composite of collagen fibrils, mineral and NCPs, which assemble together in sub-layers. According to the current model of the lamellar structure, within a single lamella, these sub-layers progressively rotate with respect to each other in a plywood-like fashion. The resulting lamella can vary in thickness from 3 up to 10 μm (Giraud-Guille, 1988; Weiner et al., 1999). Further concentric arrangement of cylindrical lamellae results in a hollow cylindrical laminate structure, known as an osteon, which surrounds a blood vessel (Fratzl and Weinkamer, 2007). In a single osteonal lamellae, the previous mentioned sub-layers rotate to an angle from roughly 10° to 60° in respect to osteon long axis (Wagermaier et al., 2006). Finally, between two subsequent lamellae lies a putatively NCP-rich (Derkx et al., 1998) interlamellar area where the mineralized collagen fibrils are oriented perpendicularly to the longitudinal axis of the osteon (Ascenzi and Benvenuti, 1986; Reid, 1986; Ziv et al., 1996). This area is often called "thin", "dense" or "transverse" lamella (Marotti, 1993; Reid, 1986), and has been characterized as a transition zone between lamellae (Ziv et al., 1996).

The first line of defence against bone fracture appears on the nanoscale, with NCP-mediated optimal load transfer between mineralized collagen fibrils (Gupta et al., 2006b). Specifically, NCPs form a matrix (soft phase) around the mineralized collagen fibrils (hard phase), which dissipates energy during fracture (Adams et al., 2008; Fantner et al., 2007; Fantner et al., 2005) and can also re-heal in a molecular

fashion (Zappone et al., 2008). The importance of NCPs for the mechanical properties of bone, has been recently pointed out (Thurner et al., 2010), but the actual way in which these proteins contribute to the fracture resistance of bone tissue is still not entirely clear.

To explain the remarkable properties of bone material and specifically its toughness and elasticity, we need to understand how optimal load transfer and energy dissipation mechanism are integrated at the various hierarchical levels. Here, we investigate the composition, structure and micromechanical role of the sub-osteonal features of bone, specifically lamellae and interlamellar areas, to uncover their role in load bearing, energy dissipation and crack propagation mechanisms. We hypothesize that the interface or transition zone between lamellae is structurally and compositionally different to lamellae. In fact, we find that what has previously been reported to as "thin" lamellae are in fact interlamellar areas with different structure and composition compared to "thick" lamellae and thus should be considered as being very much distinct from them. In addition, we find that these features interact with the lamellae in a manner analogous to engineered "elastomeric bearing pads" used in bridges (Kelly, 2002; Nakashima et al., 2004), in order to transfer load and movement. Finally, when stress concentration leads to crack initiation, the propagation of the stable crack is directed through these areas, making them a significant contributor towards fracture toughness.

2. Materials and Methods

2.1 Specimen preparation

One bovine femur was acquired from a local meat wholesaler and stored at -20 ^{o}C until further preparation. Bone samples ($n \geq 3$ for all analysis methods except EDTA where $n = 1$) were harvested from the midshaft of the femur as follows; a butcher's bandsaw (BG 200, Medoc, Logrono, Spain) and a low speed precision saw (IsoMet, Buehler, Lake Bluff, IL, USA) was used for cutting the femora into rectangular bars of 0.8 - 1.0 mm width - height and 3 cm long, oriented perpendicular to the long axis of the bone (Figure 1 – c and supplementary information). Subsequently, all samples were polished on their top side using sandpapers and diamond suspensions until a final surface roughness of ~ 1 μm was achieved. In more detail, samples were first polished using a Grit 400, 600 and 1200 (Buehler - Carbimet® Paper Disks) until a

smooth surface could be observed. The final polishing was achieved using polishing microcloths (Buehler) and a sequence of 6 μm, 3 μm and 1 μm diamond suspension polishing solutions (Buehler MetaDi® Monocrystalline Diamond Suspension). After each polishing step, the samples were immersed in an ultrasonic bath for five (5) minutes to clean the polished surface from any stacked bone powder and diamond crystal residuals.

2.2 In situ micro-tensile experiments and AFM Imaging

The samples were notched on one side using the low speed-saw, as well as a razorblade and 1 μm particulate diamond suspension (final notch radius of a few micrometers). Subsequently, sample ends were embedded in PMMA resin using a mould, producing sample ends compatible to the receptacles on a NanoRack prototype testing apparatus (Asylum Research, Santa Barbara, CA, USA), used as clamp points during micromechanical testing. *In situ* micro-mechanical tensile tests were carried out by stretching the sample (tensile loading), perpendicularly to the bone long axis, using the NanoRack prototype. In all cases, load and displacement did not exceeded 7.2 N or 0.015 mm respectively, which resulted in a maximum applied stress of 8.5 – 10.5 MPa. Images were acquired by means of an MFP3D AFM (Asylum Research) in contact mode, in air, using Au coated triangular silicon nitride probes (Olympus - TR400PSA; k = 0.08 N/m, Tip radius 20 nm).

2.3 Surface demineralization

To uncover the underlying collagen structure, polished bone surfaces were treated with 15 mMol EDTA in 5 mMol, HEPES buffer. EDTA dissolves the minerals that cover the collagen fibrils. The pH of the resulting solution was 9.5. A droplet of the solution was deposited on a sample surface where it was immobilized due to surface tension. After 360 s the sample was rinsed with ultrapure water and imaged with AFM in contact mode (Olympus - TR400PSA). Surface roughness was determined in regions of interest in the form of root mean square (R_{ms}) values using built in functions of the of the AFM control and analysis software (Asylum Research).

2.4 Cantilever-based nanoindentation

Cantilever-based nanoindentation measurements were conducted with the same setup and sample preparation as described for *in situ* micro-tensile experiment using the

Olympus OMCL-AC200TS (Olympus) cantilevers. All measurements were conducted on lamellae and interlamellar areas. Cement lines were considered as distinct osteonal features and were not included in the analysis. Lamellae and interlamellar areas were distinguished visually based on the gray level, the size of the feature (typically ~ 1 μm) and the topography as expressed by the profile analysis (cf. supplementary information). The interlamellar areas exhibited diminished resistance against wear and they always appear lower than lamellae. This was true in both perpendicularly and parallel cut samples. To avoid indenting any potential "transition zone", all measurement were performed at locations central within each feature.

Before an experiment, each sample was kept immersed in PBS and removed from the medium just before it. After imaging of the Region of Interest (ROI; Figure 2-d) in AC mode, approximately 600 ($550 \leq n \leq 625$) force-controlled (max. load = 80 nN; indentation rate = 45 nm/s) force-indentation curves were recorded on each sub-osteonal feature; namely lamellar and interlamellar areas. Next, the same procedure was repeated for both features under constant load conditions (applied load = 7 N / ~8.5 – 8.5 MPa). To achieve this, the sample was initially loaded to the desired magnitude, and when this reduced due to stress relaxation and creep effects, the sample was stressed again so that the load returned to the initial value of 7N. After repeating this procedure three or four times, the stress relaxation rate was low enough to allow imaging and indentation measurements under "constant" load conditions.

Inverse optical level sensitivity (InvOLS) and cantilever spring constant calibration were performed according to manufacturer instructions. In brief, calibration of virtual deflection in optical path was achieved by performing a force curve in air and setting the slope of that curve as the virtual deflection line (Virtual Def. Line). Next, the cantilever InvOLS was determined by performing 5 force curves against a non-deformable surface (glass slide). The gradient of the linear region of the retracted signal was measured and the mean value of the five gradients set as the cantilever InvOLS. Finally, the cantilever spring constant was determined using the thermal noise method (Sader et al., 1999). Spring constants were typically around 8 N/m and similar to the values of 9 N/m given by the manufacturer.

The projected contact surface area function for each tip was determined via imaging of a calibration grating consisting of sharp Si spikes (TGT-1, NT-MDT; cone angle 50°). A custom made Matlab (version 7.10.0.4999, The MathWorks Inc, Natick, Massachusetts) algorithm was used to reconstruct the tip shape from the acquired

image based on numerical deconvolution as proposed by Keller and Franke (Keller and Franke, 1993). The projected area function was then calculated from the reconstructed tip image, using a built-in function of the AFM control and analysis software (Asylum Research).

Finally the reduced modulus (E_r) for each curve was determined by applying the Oliver-Pharr model (Oliver and Pharr, 2004) to the unloading data (Figure 1 – b).

2.5 Statistical analysis

Statistical analysis was performed for each cantilever-based nanoindentation data set using a Wilcoxon rank sum test (significance threshold $p < 0.01$) and the normality of distributions was assessed by means of a Kolmogorov–Smirnov test in MATLAB (version 7.10.0.4999, The MathWorks Inc, Natick, Massachusetts).

2.6 Digital image correlation

The displacement map of a selected region of interest (ROI) was generated in order to visualise the strain field within the ROI where the indentation measurements had been performed. First, AFM grayscale height images were acquired from the ROI (Figure 2-d) in contact mode using the same Olympus TR400PSA cantilevers in the unloaded as well as in the loaded state. The images were then extracted in lossless (.tif) format and enlarged in Adobe Photoshope CS5 (v12 x64) using the bicubic interpolation algorithm (from initial image size 512 x 512 to 2000 x 2000 pixels). The strain map was then generated by feeding both images into commercial digital image correlation software (Vic-2D 2009, Correlated Solutions, Columbia, SC, USA). The subset size was set at 101 pixels (i.e. the number of pixels in each interrogation window) and the step size to 1.

2.7 Micro-Raman Imaging

Compositional analysis and imaging was performed by means of μ-Raman microscopy (inVia Raman microscope, Renishaw, New Mills, UK) using a 532 nm laser line. A computer controlled XYZ motorized stage moved the sample by 0.5 μm increments after every acquisition until whole 20 μm x 20μm Region of Interest (ROI) was measured. The spectra were acquired by focusing the laser beam on the sample surface via a x50 objective lens resulting a spot size of ~ 500 nm. The tightest theoretical beam diameter (D) is given by:

$$D = \frac{2 \cdot \lambda}{\pi \cdot N.A.}, (1)$$

where λ = 532 nm is the wavelength of the incident light and N.A. = 0.75 is the numerical aperture N.A. of the used lens. For these values, eq. 1 gives D = 451 nm. An exposure time of 2 sec. and a spectral resolution of 1 cm^{-1} was used in all cases. A total of 1600 spectra were record from the selected ROI, which were then further processed in order to produce the composition maps.

The Fluorescent background was removed from all raw spectra in MATLAB using a modified 5th order polynomial fit algorithm (Lieber and Mahadevan-Jansen, 2003); spectra were then smoothed for noise reduction and the intensity or the ratio of user-defined Raman peaks were measured. Finally, μ-Raman compositional images were reconstructed by assigning a grey level value to the measured intensity or ratio value (Figure 1 – a).

3. Results

3.1 Selective deformation and stiffening of interlamellar areas under load

Cantilever-based nanoindentation measurements were carried out on lamellae and interlamellar areas in unloaded and tensile loaded conditions. The statistical analysis of the nanoindentation moduli revealed a selective stiffening of interlamellar areas when loaded, which was not evident in lamellae. Measured modulus values are presented in Table 1 and Figure 2-c. It is important to note that the moduli reported here are obtained at only a few nanometers depth and hence reflect the properties of individual collagen fibrils, nanocrystals and NCPs rather than bulk bone properties.

Table 1: Reduced moduli of lamellae and interlamellar areas in both loaded and unloaded conditions determined from cantilever-based nanoindentation.

		Reduced Modulus (GPa)		
		Median	*Mean*	*SE of Mean*
Unloaded	*Lamella*	1.89	2.13	0.05
	Interlamellar Area	1.47	1.79	0.06
Loaded	*Lamella*	1.95	2.67	0.09
	Interlamellar Area	2.10	2.79	0.08

Without any load acting on the sample, lamellae showed a significantly higher reduced modulus in comparison to interlamellar areas (p-value << 0.01). Applying tensile load results in a significant increment of the measured reduced modulus (E_r) of interlamellar areas (p-value << 0.01), while the modulus of lamellae shows a similar but insignificant trend (p-value > 0.01). Loading also reversed the significant difference between the two moduli (p-value > 0.01); with interlamellar areas being stiffer than lamellae, revealing a selective stiffening of interlamellar areas.

Due to the nanometre-size tip radius and the shallow indentation depths applied, the cantilever-based nanoindentation experiments probe the mechanical behaviour of mineralized collagen fibrils and their surrounding mineralized NCP matrix. Under load, mineralized collagen fibrils are pulled apart, exposing the stretched NCP matrix to the tip. Consequently, a longer tail towards higher *Er* values appears in both lamellar and interlamellar area distributions, which causes the stretching of the corresponding box plots (Figure 2 - c).

Height (topographical) AFM images taken prior to- and at a loaded state were used to assess local strains by means of a digital image correlation (DIC) technique. As shown on the contour map of the principal strain 1 in Figure 2 - b, the interlamellar areas (noted with stars) take over a considerable amount of the applied strain. This phenomenon is presented in greater detail in Figure 3, where the different behaviour of lamellae and interlamellar areas under isostress and isostrain conditions are illustrated. In the first case (load perpendicular the long axis of the osteon), interlamellar areas gradually develop higher microstrains with increased load, while lamellae remain rather unaffected (Figure 3). This is not the case when loading is parallel to the osteons long axis (parallel plane). In this case, as the two microfeatures are under isostrain conditions, no difference in microstrain development can be seen between the lamellae and the interlamellar areas.

3.2 Interlamellar areas are collagen-deficient and NCP-rich

Local composition was studied using μ-RAMAN microscopy. Figure 4 shows the peak intensity maps of (a) the Amide I (C = O stretching vibration; 1669 cm^{-1} (Movasaghi et al., 2007)), which mainly corresponds to the collagenous matrix (Kazanci et al., 2007), (b) the ν_1PO_4 vibrational mode of the mineral compound (960 cm^{-1}), (c) the C-H – bending (1458 cm^{-1}), which corresponds to both collagen and NCPs (Kazanci et al., 2007) and finally (d) the ratio of Amide I / C-H – bending.

Given that Amide I is almost exclusively due to the collagenous matrix, while both collagens and NCPs are contributing to the C-H – bending intensity (Kazanci et al., 2007), the ratio of these peaks serves as a measure of their relative concentrations. Higher ratio means higher collagen or lower NCP concentration, and vice versa. Importantly, our results show that interlamellar areas exhibit a decrease in Amide I intensity as well as in the Amide I / C-H-bending ratio, implying that they are collagen deficient and NCP-rich.

No difference was detected with respect to the degree of mineralization between lamellae and interlamellar areas. Finally, μ-RAMAN microscopy uncovered the underlying canalicular structures that were not visible underneath the light microscope.

3.3 NCP-rich interlamellar areas relevant for fracture toughness

Micromechanical experiments reveal that cracks preferentially propagate through interlamellar areas (cf. Figure 5 and Supplementary video V1), even when they are oriented perpendicular to the principal crack path and in line with the crack-opening displacement. By use of *in situ* micromechanical testing of bovine bone samples during AFM imaging (cf. supplementary information), we have imaged crack propagation within the sub-osteonal features in a time-lapsed fashion. Interestingly, interlamellar areas appear equally mineralised compared to the lamellae, yet cracks preferably propagate through the interlamellar areas, as mentioned above as. This means that mineral concentration alone is not a strong crack path predictor at this level.

3.4 Interlamellar areas are clearly distinct features compared to lamellae

In addition to composition, the orientation of mineralized collagen fibrils can also influence crack propagation. AFM imaging reveals that collagen fibrils are predominantly normal to the long bone axis in interlamellar areas while this is not the case for lamellae. To uncover collagen fibril orientation, samples were treated with ethylene-ediaminetetraacetic acid (EDTA) (cf. supplementary information). AFM imaging of EDTA-treated surfaces revealed the underlying microstructure, i.e. osteocyte lacunae, the canalicular network, as well as the interlamellar areas, as shown in Figure 6. These experiments show that interlamellar areas are clearly distinct features compared to lamellae, in terms of structure and morphology.

Lamellae appeared rougher than interlamellar areas after EDTA treatment (cf. Figure 6), due to predominantly vertical or standing orientation of collagen fibrils. Also there appeared to be a rather sharp delineation of lamellae and interlamellar areas. Average roughness R_{ms} analysis on EDTA treated bone sample revealed a difference of 48.4 % between lamellae and interlamellar areas, with lamellae being rougher ($R_{ms\_Lamellae}$ = 66.2 ± 9.3 nm / $R_{ms\_InterlamellarArea}$ = 34.2 ± 1.9 nm). Mineral removal in the interlamellar areas uncovered lying (rather than standing) collagen fibrils (Figure 6).

4. Discussion

Here, via *in situ* mechanical testing during AFM, we show that crack propagation in cortical bone preferentially occurs in interlamellar areas (Figure 5); also called thin lamellae. The assumption that lamellar interfaces provide a propagation path of least resistance has previously been reported (Fratzl, 2008; Jepsen et al., 1999; Peterlik et al., 2005). However, to the best of our knowledge, stable crack propagation on the sub-osteonal / lamellar level, resolving bone micro- and nanostructure, has not been captured so far. Cantilever-based nanoindentation experiments revealed that these interlamellar areas are less stiff compared to lamellae, but stiffen selectively under tensile load as shown in Figure 2. Image analysis (DIC) reveals that there is higher deformation accompanying this stiffening process (Figure 3). Chemical treatment and AFM imaging revealed a change in collagen orientation in the interlamellar areas (Figure 7), where fibrils are developed circumferentially around the Haversian canal. This is in contrast with the lamellae, where the fibrils have been reported to be arranged in cholesteric layers with respect to osteon long axis (Wagermaier et al., 2006). Furthermore, a lower content of collagen and/or a higher content of NCPs is determined by means of μ-Raman imaging (Figure 4) on these areas. Interestingly, mineral density was unchanged across the lamellar / interlamellar areas.

Bone toughening mechanisms have been the focus of bone research for many years. So far, the remarkable fracture resistance of bone tissue has been attributed to numerous toughening mechanisms, load bearing and energy dissipation mechanisms among them, spanning all bone hierarchical levels (Gupta et al., 2006b; Peterlik et al., 2005). On the molecular level, stretching of the NCP meshworks results in the breakage of ion-mediated bonds between the NCP molecules (Gupta et al., 2006b). Zappone et al. show that this mechanism can dissipate considerable amount of energy

(Zappone et al., 2008). This mechanism is also present in bone on the nanoscale; the NCP meshwork/matrix acts as an adhesion medium between mineralized collagen fibrils dissipating energy in a similar manner, and facilitating load transfer between the subsequent fibres (Gupta et al., 2006b; Gupta et al., 2005). It has been estimated that less than 1% per weight of this matrix ("glue") is enough to provide bone with its known yield strength (~150 MPa) (Fantner et al., 2005). From the fractographic standpoint, it has been shown that cracks are formed when these interfaces fail (Thurner et al., 2009). Crack propagation, and consequently the fracture toughness of the tissue, is to a large extent affected by features of higher hierarchical levels, such as lamellae, interlamellar areas as well as cement lines and osteons. These features are responsible for a multitude of toughening mechanisms which include crack deflection and microdamage formation (Peterlik et al., 2005). While the importance of load transfer mechanisms has been studied and discussed for the nanoscale, such mechanisms have not been reported or discussed for the osteonal and sub-osteonal level, which largely influence crack propagation (Fratzl, 2008; Vashishth, 2007).

From our study we propose a load transfer mechanism within the sub-osteonal features of bone, which involves the cooperative deformation of "softer" interlamellar areas and "harder" lamellae and thereby dissipation of energy in a reversible manner. Sequential combination of hard and soft phase has previously been proven to reinforce toughness and strength of both nature and engineering materials (Espinosa et al., 2011; Naraghi et al.). Similar structures, combining soft deformable materials with hard and rigid ones, can also be found in civil engineering structures. Elastomeric seismic isolation bearing pads are commonly used to protect structures, like buildings or bridges, from catastrophic failure when relative translation and/or rotation of the structure/deck against the ground are needed. The deformation of the elastomeric bearing pads protects the structure by accommodating movement while also dissipating energy (Kelly, 2002; Nakashima et al., 2004). In an analogous way, the NCP-rich interlamellar areas -*soft phase*- assist the transfer of load between sequential lamellae acting as elastomeric, or perhaps even as, "elasto-plastic" bearing interfaces. Obviously the effect in bone is much less dramatic compared to a combination of concrete and rubber – yet it is very likely to be an important contributor to toughness. We propose that the "lamella | interlamellar area | lamella" deformation mechanism is the microstructural level equivalent of the "mineralized collagen fibril | interfibrillar "glue layer" | mineralized collagen fibril" mechanism

found at the nanostructural level (Gupta et al., 2007). It is important to note that the microscale mechanism relies on the combination of changes in composition as well as structure in interlamellar areas and depends on the properties and interplay of all constituents of bone matrix, i.e. mineral, collagen and NCPs .The induced strain is taken over by the NCP-rich (and collagen-deficient) interlamellar areas, by means of a multilevel mechanism, and it is transferred along the sequential lamellae. In the sub-osteonal level, the looser packing of mineralized collagen fibrils allows interlamellar areas for larger deformations (Figure 2 - b) and is also the reason why these interfaces are found to be more compliant than the lamellae (Gupta et al., 2006a). On the nanoscale, the interfibrillar NCP meshwork between the loosely-packed collagen fibrils are stretched apart, also stretching the interfibrillar NCP matrix (Figure 7).

This "lamella | interlamellar area | lamella" deformation mechanism and its compositional and structural origin also explains why interlamellar areas appear to have a lower reduced modulus (E_r). This difference becomes marginal when bone is under load, i.e. when pulling apart the mineralized collagen fibrils, "exposing" the stretched inter-fibrillar NCP meshwork to the tip (supplementary Figure S5). Thus, a higher reduced modulus, in comparison to the unloaded case, is observed. During the stretching of the interlamellar areas, likely sacrificial bonds within the NCP meshwork are breaking, exposing hidden length (Fantner et al., 2005). This would aid in dissipation of energy, based on entropic elasticity rather than elastic energy, in the stretched interlamellar areas (Figure 7). After the elimination of the applied load, or upon crack closure, the NCP meshwork is relaxed and intra- and intermolecular NCP bonds could reform (Fantner et al., 2007), restoring the mechanical integrity of interlamellar area partly or even in full. This might be a way for osteons to allow and withstand various modes of micro-deformation without inducing damage.

Like articular cartilage (Loparic et al., 2010), bone is a nanocomposite material built from components with different mechanical properties (i.e. individual mineralized collagen fibrils and mineralized non-collagenous protein matrix). The nanometer-size tip radius (~7 – 15 nm) of the AFM probes, used for cantilever-based nanoindentation, allows probing the mechanical behaviour of fundamental components of lamellae and interlamellar areas. This also explains why the moduli values reported here are an order of magnitude smaller than ones we previously reported on the tissue level (Szabó et al., 2011). Conventional nanoindentation assesses the overall feature behaviour of, for example, a lamella and its vicinity to the

applied load (Loparic et al., 2010). To validate the cantilever-based nanoindentation, measurements of two more experiments were conducted to serve as "controls". Two well-characterised materials, that is, Poly(methyl methacrylate) - (PMMA); and Polystyrene – (PP) were measured and analysed with the exact same experimental procedure used for the bone samples. The analysis of the results for both materials returned the values of 4.5 ± 0.14 and 1.36 ± 0.02 GPa for the PMMA and PP respectively, which are similar to the values reported in the literature for these materials (Jee and Lee, 2010; Pukánszky et al., 1997), when measured using conventional nanoindentation (5.2 ± 0.5 and 2.0 ± 0.4 GPa for PMMA and PP respectively; data not shown).

Our results let us speculate that the increased bone fragility found in NCP deficient bones (Thurner et al., 2010) could be due to the lack of such dissipation mechanisms; during failure, crack propagation is influenced by the laminated structure of the osteon (Koester et al., 2008) or lamellar bone, similar to hybrid composite materials (Ming-Yuan and Hutchinson, 1989). In tensile loading, crack growth predominantly occurs within the "soft" interlamellar areas. The concentric arrangement of "hard" lamellae into an osteonal structure deflects the transverse cracks from their path, in this way protecting the nerve and vessels enclosed in the Haversian canal (Gupta et al., 2006a). Under transverse compression (with respect to Haversian canal) extensive cross-hatched damage has been observed in the osteonal level, which at the single-osteon level consists of groups of intralamellar arc-shaped microcracks. These microcracks develop in areas of high shear, at approximately – 45^{o} and + 45^{o} from loading direction, and follow the curvature of lamellae (Ebacher et al., 2011; Ebacher and Wang, 2009). The softer and more deformable interlamellar areas appear to be able to withstand the introduced shear, maintaining their structural integrity and transferring load from one lamella to the other. Furthermore, while the less stiff interlamellar areas widen or are sheared upon complex load modes, they might also serve as a "shock absorbing" mechanism, storing elastic energy during impact via compression of the NCP meshwork.

With regards to the μ-RAMAN results presented, it is important to note that the Amide I peak is not only dependent on collagen concentration, but also orientation (Kazanci et al., 2006). Lying or standing of collagen fibrils could modulate the signal intensity. However, control experiments, in which μ-RAMAN imaging was done on a parallel section with respect to osteon long axis, where the collagen fibrils are

standing rather than lying, revealed a similar drop in intensity on the interlamellar areas (cf. supplementary information, Figure S4). Furthermore, it is known that Raman scattering intensity of Hydroxyapatite is dependent on the c-axis orientation of the crystal (Tsuda and Arends, 1994) and that the mineral crystals mainly lie with their c-axis parallel to the collagen fibrils (Sasaki et al., 1989). Thus, if the observed intensity-drop was only dependent on collagen orientation, a similar drop should have been observed in ν_1PO_4 vibrational mode of the mineral compound which is known to be highly sensitive to orientation direction (Kazanci et al., 2006; Kazanci et al., 2007). Such a drop is not evident in the ν_1PO_4 mode intensity maps suggesting that the drop observed in Amide I, is mainly due to concentration difference.

There are a few further experimental limitations of this study. In the case of micro-tensile experiments, bone samples were dry, which is known to significantly affect the elastic modulus and the stiffness of the tissue (Hengsberger et al., 2002; Rho and Pharr, 1999). Nevertheless, bone failure behaviour has been reported to be governed by the same mechanisms in both dry and wet samples (Braidotti et al., 2000a; Braidotti et al., 1997a). In more detail, despite the differences in energy absorption and ductility, both conditions exhibit fibre/matrix debonding and delamination-like failure. Our microtensile experiments capture this very delamination phenomenon and confirm, in a time-lapsed fashion, that interlamellar areas indeed provide a preferential crack propagation path (Peterlik et al., 2005). A similar argument could also be raised with respect to the cantilever-based nanoindentation results. We believe, though, that it is reasonable to consider the sample surface to be only partially dehydrated (a) as samples were immersed in PBS until the time when the experiments were conducted and (b) due to the presence of a water-film (condensed from the atmosphere) on the sample's surface. In addition, as interlamellar areas are NCP-rich, it should be expected that under physiological conditions they are more hydrated than lamellae (Braidotti et al., 2000a). Thus, it may be that dehydration partially masks their selective stiffening behaviour, which may be more vivid under physiological conditions. The same stands for the Digital Image Correlation study as it is known that dehydration affects the "weak" lamellar interfaces which are playing a crucial role in the deformation mechanism (Seto et al., 2008). Finally, the DIC results presented above only provide qualitative information about the strain distribution. Nevertheless, they confirm higher strain in interlamellar areas, which is also evident from displacement fields; further, more sophisticated experiments are required to

reduce inherent issues such as scanner drift in the slow scan axis. Also, higher resolution and contrast AFM images could improve the resulted strain maps as they would enhance the salient features of the image used for the DIC analysis.

In summary, our results show that lamellar interfaces, i.e. interlamellar areas, are features with compositional and structural differences from lamellae; they are collagen-deficient, NCP-rich and have different collagen fibril orientation in comparison to lamellae. Interlamellar areas act as crack guidance zones and deflectors. Additionally, we find that they allow for micromotion in bone likely without permanent damage formation, partly similar to mechanisms found on the nanoscale. Structurally, from the nanoscale through the microscale and all the way up to the macroscale, bone adaptation to the complex biological loading conditions seems governed by hard/soft phase interaction, to achieve reversible elasto-plastic deformation prior to true damage formation. Small changes on the nano- or microstructural level disturbing the hard/soft phases, such as NCP deficiency in the bone tissue, due to age or disease could affect bone ability to propagate such mechanisms. This could lead to lowered fracture toughness and overall mechanical competence of bone.

Acknowledgments

We are grateful to Prof. Mark Taylor, Dr. Martin Stolz, Dr. Jurgita Zekonyte and Dr. Sofia Michopoulou for the fruitful discussions during the writing of this manuscript, and Ms Gwen Palmer for text editing-proofing. The authors would also like to acknowledge the Faculty of Engineering and the Environment of the University of Southampton - UK, Asylum Research and EPSRC for the financial support of this study.

References

Adams, J., Fantner, G., Fisher, L., Hansma, P., 2008. Molecular energy dissipation in nanoscale networks of dentin matrix protein 1 is strongly dependent on ion valence. Nanotechnology 19, 384008.

Ascenzi, A., Benvenuti, A., 1986. Orientation of collagen fibers at the boundary between two successive osteonic lamellae and its mechanical interpretation. J. Biomech. 19, 455-463.

Braidotti, P., Bemporad, E., D'alessio, T., Sciuto, S., Stagni, L., 2000a. Tensile experiments and SEM fractography on bovine subchondral bone. J. Biomech. 33, 1153-1157.

Braidotti, P., Bemporad, E., D'Alessio, T., Sciuto, S.A., Stagni, L., 2000b. Tensile experiments and SEM fractography on bovine subchondral bone. J Biomech 33, 1153-1157.

Braidotti, P., Branca, F., Stagni, L., 1997a. Scanning electron microscopy of human cortical bone failure surfaces. J. Biomech. 30, 155-162.

Braidotti, P., Branca, F.P., Stagni, L., 1997b. Scanning electron microscopy of human cortical bone failure surfaces. J Biomech 30, 155-162.

Bukhari, M., 2009. The National Osteoporosis Guideline Group's new guidelines: what is new? Rheumatology.

Cowin, S.C., 2001. Bone mechanics handbook. CRC press USA.

Currey, J., 1984. Effects of differences in mineralization on the mechanical properties of bone. Philosophical Transactions of the Royal Society of London. B, Biological Sciences 304, 509-518.

Derkx, P., Nigg, A., Bosman, F., Birkenhäger-Frenkel, D., Houtsmuller, A., Pols, H., Van Leeuwen, J., 1998. Immunolocalization and quantification of noncollagenous bone matrix proteins in methylmethacrylate-embedded adult human bone in combination with histomorphometry. Bone 22, 367-373.

Ebacher, V., Guy, P., Oxland, T.R., Wang, R., 2011. Sub-Lamellar Microcracking and Roles of Canaliculi in Human Cortical Bone. Acta Biomater.

Ebacher, V., Wang, R., 2009. A unique microcracking process associated with the inelastic deformation of Haversian bone. Adv. Funct. Mater. 19, 57-66.

Espinosa, H.D., Juster, A.L., Latourte, F.J., Loh, O.Y., Gregoire, D., Zavattieri, P.D., 2011. Tablet-level origin of toughening in abalone shells and translation to synthetic composite materials. Nat. Commun. 2, 173.

Eyre, D., Dickson, I., Van Ness, K., 1988. Collagen cross-linking in human bone and articular cartilage. Age-related changes in the content of mature hydroxypyridinium residues. Biochem. J. 252, 495.

Fantner, G.E., Adams, J., Turner, P., Thurner, P.J., Fisher, L.W., Hansma, P.K., 2007. Nanoscale ion mediated networks in bone: osteopontin can repeatedly dissipate large amounts of energy. Nano Lett. 7, 2491-2498.

Fantner, G.E., Hassenkam, T., Kindt, J.H., Weaver, J.C., Birkedal, H., Pechenik, L., Cutroni, J.A., Cidade, G.A.G., Stucky, G.D., Morse, D.E., 2005. Sacrificial bonds and hidden length dissipate energy as mineralized fibrils separate during bone fracture. Nat. Mater. 4, 612-616.

Felsenberg, D., Boonen, S., 2005. The bone quality framework: determinants of bone strength and their interrelationships, and implications for osteoporosis management. Clin. Ther. 27, 1-11.

Fratzl, P., 2008. Bone fracture: When the cracks begin to show. Nat. Mater. 7, 610.

Fratzl, P., Gupta, H., Paschalis, E., Roschger, P., 2004. Structure and mechanical quality of the collagen–mineral nano-composite in bone. J. Mater. Chem. 14, 2115-2123.

Fratzl, P., Weinkamer, R., 2007. Nature's hierarchical materials. Progress in Materials Science 52, 1263-1334.

Giraud-Guille, M., 1988. Twisted plywood architecture of collagen fibrils in human compact bone osteons. Calcif. Tissue Int. 42, 167-180.

Gupta, H., Stachewicz, U., Wagermaier, W., Roschger, P., Wagner, H., Fratzi, P., 2006a. Mechanical modulation at the lamellar level in osteonal bone. J. Mater. Res. 21, 1913-1921.

Gupta, H.S., Fratzl, P., Kerschnitzki, M., Benecke, G., Wagermaier, W., Kirchner, H.O.K., 2007. Evidence for an elementary process in bone plasticity with an activation enthalpy of 1 eV. J. Royal Soc. Interface 4, 277.

Gupta, H.S., Seto, J., Wagermaier, W., Zaslansky, P., Boesecke, P., Fratzl, P., 2006b. Cooperative deformation of mineral and collagen in bone at the nanoscale. Proceedings of the National Academy of Sciences 103, 17741.

Gupta, H.S., Wagermaier, W., Zickler, G.A., Aroush, D.R.B., Funari, S.S., Roschger, P., Wagner, H.D., Fratzl, P., 2005. Nanoscale deformation mechanisms in bone. Nano Lett. 5, 2108-2111.

Hamed, E., Lee, Y., Jasiuk, I., 2010. Multiscale modeling of elastic properties of cortical bone. Acta Mechanica 213, 131-154.

Hengsberger, S., Kulik, A., Zysset, P., 2002. Nanoindentation discriminates the elastic properties of individual human bone lamellae under dry and physiological conditions. Bone 30, 178-184.

Hui, S.L., Slemenda, C.W., Johnston Jr, C.C., 1988. Age and bone mass as predictors of fracture in a prospective study. J. Clin. Investig. 81, 1804.

Jee, A.Y., Lee, M., 2010. Comparative analysis on the nanoindentation of polymers using atomic force microscopy. Polym. Test. 29, 95-99.

Jepsen, K.J., Davy, D.T., Krzypow, D.J., 1999. The role of the lamellar interface during torsional yielding of human cortical bone. J. Biomech. 32, 303-310.

Jepsen, K.J., Pennington, D.E., Lee, Y.L., Warman, M., Nadeau, J., 2001. Bone brittleness varies with genetic background in A/J and C57BL/6J inbred mice. J. Bone Miner. Res. 16, 1854-1862.

Kanis, J.A., Borgstrom, F., De Laet, C., Johansson, H., Johnell, O., Jonsson, B., Oden, A., Zethraeus, N., Pfleger, B., Khaltaev, N., 2005. Assessment of fracture risk. Osteoporos. Int. 16, 581-589.

Kavukcuoglu, N.B., Denhardt, D.T., Guzelsu, N., Mann, A.B., 2007. Osteopontin deficiency and aging on nanomechanics of mouse bone. Journal of Biomedical Materials Research Part A 83, 136-144.

Kazanci, M., Roschger, P., Paschalis, E., Klaushofer, K., Fratzl, P., 2006. Bone osteonal tissues by Raman spectral mapping: orientation-composition. J. Struct. Biol. 156, 489-496.

Kazanci, M., Wagner, H., Manjubala, N., Gupta, H., Paschalis, E., Roschger, P., Fratzl, P., 2007. Raman imaging of two orthogonal planes within cortical bone. Bone 41, 456-461.

Keller, D., Franke, F., 1993. Envelope reconstruction of probe microscope images. Surface Science 294, 409-419.

Kelly, J.M., 2002. Seismic isolation systems for developing countries. Earthquake spectra 18, 385.

Koester, K.J., Ager, J., Ritchie, R., 2008. The true toughness of human cortical bone measured with realistically short cracks. Nat. Mater. 7, 672-677.

LeGeros, Z., 1981. Apatites in biological systems. Progress in Crystal Growth and Characterization 4, 1-45.

Lieber, C.A., Mahadevan-Jansen, A., 2003. Automated method for subtraction of fluorescence from biological Raman spectra. Appl. Spectrosc. 57, 1363-1367.

Loparic, M., Wirz, D., Daniels, A., Raiteri, R., VanLandingham, M.R., Guex, G., Martin, I., Aebi, U., Stolz, M., 2010. Micro-and Nanomechanical Analysis of Articular Cartilage by Indentation-Type Atomic Force Microscopy: Validation with a Gel-Microfiber Composite. Biophys. J. 98, 2731-2740.

Marotti, G., 1993. A new theory of bone lamellation. Calcif. Tissue Int. 53, 47-56.

Ming-Yuan, H., Hutchinson, J.W., 1989. Crack deflection at an interface between dissimilar elastic materials. International Journal of Solids and Structures 25, 1053-1067.

Movasaghi, Z., Rehman, S., Rehman, I.U., 2007. Raman spectroscopy of biological tissues. Appl. Spectrosc. Rev. 42, 493-541.

Nakashima, M., Pan, P., Zamfirescu, D., Weitzmann, R., 2004. Post-Kobe approach for design and construction of base-isolated buildings. Journal of Japan Association for Earthquake Engineering 4.

Naraghi, M., Filleter, T., Moravsky, A., Locascio, M., Loutfy, R.O., Espinosa, H.D., A Multiscale Study of High Performance Double-Walled Nanotube- Polymer Fibers. ACS Nano, 2212-2215.

Nyman, J.S., Reyes, M., Wang, X., 2005. Effect of ultrastructural changes on the toughness of bone. Micron 36, 566-582.

Oliver, W., Pharr, G., 2004. Measurement of hardness and elastic modulus by instrumented indentation: Advances in understanding and refinements to methodology. J. Mater. Res 19.

Peterlik, H., Roschger, P., Klaushofer, K., Fratzl, P., 2005. From brittle to ductile fracture of bone. Nat. Mater. 5, 52-55.

Pukánszky, B., Mudra, I., Staniek, P., 1997. Relation of crystalline structure and mechanical properties of nucleated polypropylene. Journal of Vinyl and Additive Technology 3, 53-57.

Reid, S.A., 1986. A study of lamellar organisation in juvenile and adult human bone. Anat. Embryol. 174, 329-338.

Rho, J.Y., Kuhn-Spearing, L., Zioupos, P., 1998. Mechanical properties and the hierarchical structure of bone. Med. Eng. Phys. 20, 92-102.

Rho, J.Y., Pharr, G.M., 1999. Effects of drying on the mechanical properties of bovine femur measured by nanoindentation. J. Mater. Sci.: Mater. Med. 10, 485-488.

Riggs, B., Melton, L., 1995. The worldwide problem of osteoporosis: insights afforded by epidemiology. Bone 17, S505-S511.

Roach, H., 1994. Why does bone matrix contain non-collagenous proteins? The possible roles of osteocalcin, osteonectin, osteopontin and bone sialoprotein in bone mineralisation and resorption. Cell Biol. Int. 18, 617-628.

Sader, J.E., Chon, J.W.M., Mulvaney, P., 1999. Calibration of rectangular atomic force microscope cantilevers. Rev. Sci. Instrum. 70, 3967.

Sasaki, N., Matsushima, N., Ikawa, T., Yamamura, H., Fukuda, A., 1989. Orientation of bone mineral and its role in the anisotropic mechanical properties of bone--transverse anisotropy. J. Biomech. 22, 157-159, 161-164.

Seto, J., Gupta, H.S., Zaslansky, P., Wagner, H.D., Fratzl, P., 2008. Tough lessons from bone: extreme mechanical anisotropy at the mesoscale. Adv. Funct. Mater. 18, 1905-1911.

Szabó, M., Zekonyte, J., Katsamenis, O., Taylor, M., Thurner, P., 2011. Similar damage initiation but different failure behavior in trabecular and cortical bone tissue. J. Mech. Behav. Biomed. Mater.

Thurner, P., Lam, S., Weaver, J., Morse, D., Hansma, P., 2009. Localization of phosphorylated serine, osteopontin, and bone sialoprotein on mineralized collagen fibrils in bone. J. Adhes 85, 526–545.

Thurner, P.J., Chen, C.G., Ionova-Martin, S., Sun, L., Harman, A., Porter, A., Ager III, J.W., Ritchie, R.O., Alliston, T., 2010. Osteopontin deficiency increases bone fragility but preserves bone mass. Bone 46, 1564-1573.

Tsuda, H., Arends, J., 1994. Orientational micro-Raman spectroscopy on hydroxyapatite single crystals and human enamel crystallites. J. Dent. Res. 73, 1703.
Ulrich, D., Hildebrand, T., Van Rietbergen, B., Müller, R., Rüegsegger, P., 1997a. The quality of trabecular bone evaluated with micro-computed tomography, FEA and mechanical testing. Stud. Health Technol. Inform. 40, 97-112.
Ulrich, D., Hildebrand, T., Van Rietbergen, B., Müller, R., Rüegsegger, P., 1997b. The quality of trabecular bone evaluated with micro-computed tomography, FEA and mechanical testing. Stud. Health Technol. Inform., 97-112.
Vashishth, D., 2007. Hierarchy of bone microdamage at multiple length scales. International journal of fatigue 29, 1024-1033.
Vaughan, T., McCarthy, C., McNamara, L., 2012. A three-scale finite element investigation into the effects of tissue mineralisation and lamellar organisation in human cortical and trabecular bone. J. Mech. Behav. Biomed. Mater.
Viguet-Carrin, S., Garnero, P., Delmas, P., 2006. The role of collagen in bone strength. Osteoporos. Int. 17, 319-336.
Wagermaier, W., Gupta, H., Gourrier, A., Burghammer, M., Roschger, P., Fratzl, P., 2006. Spiral twisting of fiber orientation inside bone lamellae. Biointerphases 1, 1.
Weiner, S., Traub, W., Wagner, H.D., 1999. Lamellar bone: structure-function relations. J. Struct. Biol. 126, 241-255.
Weiner, S., Wagner, H.D., 1998. The material bone: structure-mechanical function relations. Annual Review of Materials Science 28, 271-298.
Zappone, B., Thurner, P.J., Adams, J., Fantner, G.E., Hansma, P.K., 2008. Effect of Ca2+ ions on the adhesion and mechanical properties of adsorbed layers of human osteopontin. Biophys. J. 95, 2939-2950.
Zioupos, P., Currey, J., 1998. Changes in the stiffness, strength, and toughness of human cortical bone with age. Bone 22, 57-66.
Ziv, V., Sabanay, I., Arad, T., Traub, W., Weiner, S., 1996. Transitional structures in lamellar bone. Microsc. Res. Tech. 33, 203-213.

Additional information

Supplementary Information accompanies this paper

Figure Captions

Figure 1: (a) Typical Raman spectrum obtained from bovine cortical bone tissue, showing the raw (dashed black line) and corrected (solid orange line) spectrum after the fluorescent background (dashed green line) subtraction. The polynomial curve, representing the background was independently calculated for every single spectrum (b) Typical Force – Indentation curve obtained from the ROI. The unloading part (green stars) of the Force – Indentation curve (black circles) was selected for the analysis and contact depth (h_f) was approximated from the fitted curve (orange line) according to the Oliver-Pharr model. (c) Bovine cortical bone specimen used for in situ uniaxial tension experiments during AFM imaging.

Figure 2: (a) AFM height image of part of an osteon where indentation measurements were carried out. Interlamellar areas are denoted with stars (*); resolution 29 nm/pixel (b) Contour map of principal microstrains (e_1) induced by loading the bone sample, the loading direction is indicated by the green arrows. Higher microstrains appear upon the interlamellar areas revealing their elastomeric bearing–like behaviour under tension. (c) Reduced moduli obtained from the force/indentation curves for the two sub-osteonal features. With no load present, lamellae exhibit significantly higher modulus (Er) than interlamellar areas (p-value < 0.01). Loading the tissue eliminated the difference between the moduli (Er) of lamellar and interlamellar areas with interlamellar areas being marginally stiffer than lamellae, i.e. resulting in a selective stiffening of the latter during loading. (d) Optical microscopy image of a single osteon and localization of the ROI selected for the indentation experiments.

Figure 3:

DIC analysis of bovine osteonal cortical bone for both isostress and isostrain conditions, with respect to lamellae and interlamellar areas. The specimen shown in the left column is cut in the transverse plane where the long axis of the osteon perpendicular to the specimen surface. The specimen shown in the right column is cut in the parallel plane with the long axis of the osteon parallel to the specimen surface. White arrows indicate the interlamellar areas and the red ones the load direction. In the case of isostress loading, higher strains are developed gradually on interlamellar areas with increasing load. This is not evident in isostrain, loading where a more homogenous strain distribution along the lamellae and interlamellar areas. Window size 15 x 15 μm; resolution of AFM images 29 nm/pixel.

Figure 4: Superposition of μ-RAMAN intensity maps of (a) Amide I , (b) ν_1 PO4, (c) C-H –bending and (d) Amide I / C-H – bending ratio on light microscopic images. Superposition of AFM image is also presented in Figure (d). The lamellar structure is clearly visible on μ-RAMAN maps of both (a) and (d) demonstrating collagen deficiency in interlamellar areas. The intensity variation/contrast between lamellae and interlamellar areas of C-H –bending in picture (c) is less vivid. This implies that due to the collagen deficiency in interlamellar areas other biomolecules, i.e. NCPs, with C-H bonds are present. No difference of the degree of mineralization between lamella and interlamellar areas can be seen (b), but it seems the high contrast present is due to underlying canaliculi.

Figure 5: Cracks in cortical bone preferentially propagate through cement lines and interlamellar areas (a & b). Inserts i, ii and iii in (a) are time-lapsed AFM images of stable crack propagation (also see Supplementary video V1). Even when the orientation of the interlamellar areas is perpendicular to the principal crack path and in-line with the crack-opening displacement (b), cracks propagate partially through the interlamellar area. Direction of the applied load is parallel to the horizontal edges of all figures. Resolution of AFM images: (a) 55 nm/pixel, (b) 40 nm/pixel

Figure 6: (a - c top: height channel, a – c middle: amplitude channel) AFM images of the EDTA-treated osteon reveal micro-structural features such as osteocyte lacunae, the canalicular network and lamellar interfaces. (d) Localisation of the AFM imaged area with respect to osteonal canal. (e) Roughness analysis of lamella (red boxes) and interlamellar areas (green boxes). Rougher lamellar surface is most likely due to predominantly vertical or standing orientation of collagen fibrils. In contrast, collagen fibrils appear lying circumferentially with respect to the long axis of the osteon within the interlamellar areas. (f) 3D reconstruction of c. On the interlamellar area, note the absence of crater-like structures present in lamellae which correspond to standing fibrils from which the interfibrillar mineralised matrix have been removed. Also note the lying collagen fibrils, with the characteristic 67 nm banding.

Figure 7: Proposed bottom-up model of a mammalian osteon. Mineralized collagen fibrils, glued together via a mineralized NCP “glue layer”, are the building block of both lamellae and interlamellar areas. Upon tension, interlamellar areas are taking over a larger amount of the applied strain. There, the NCPs, filling the space between the loosely packed collagen fibrils, are stretched apart and sacrificial bonds (black dots - magnifying glass) start breaking (red dots - magnifying glass), releasing more hidden length. This mechanism (a) could dissipate significant amount of energy (b), allows small deformation between lamellae and (c) is reversible. This would allow osteons to withstand various modes of micro-deformation, without crack formation, propagation or failure, while at the same time dissipating energy via a reversible mechanism. Images resolution: (a): 88 nm / pixel; (b): 20 nm/pixel; (c),(e) and (f):10 nm/pixel

Figure 1

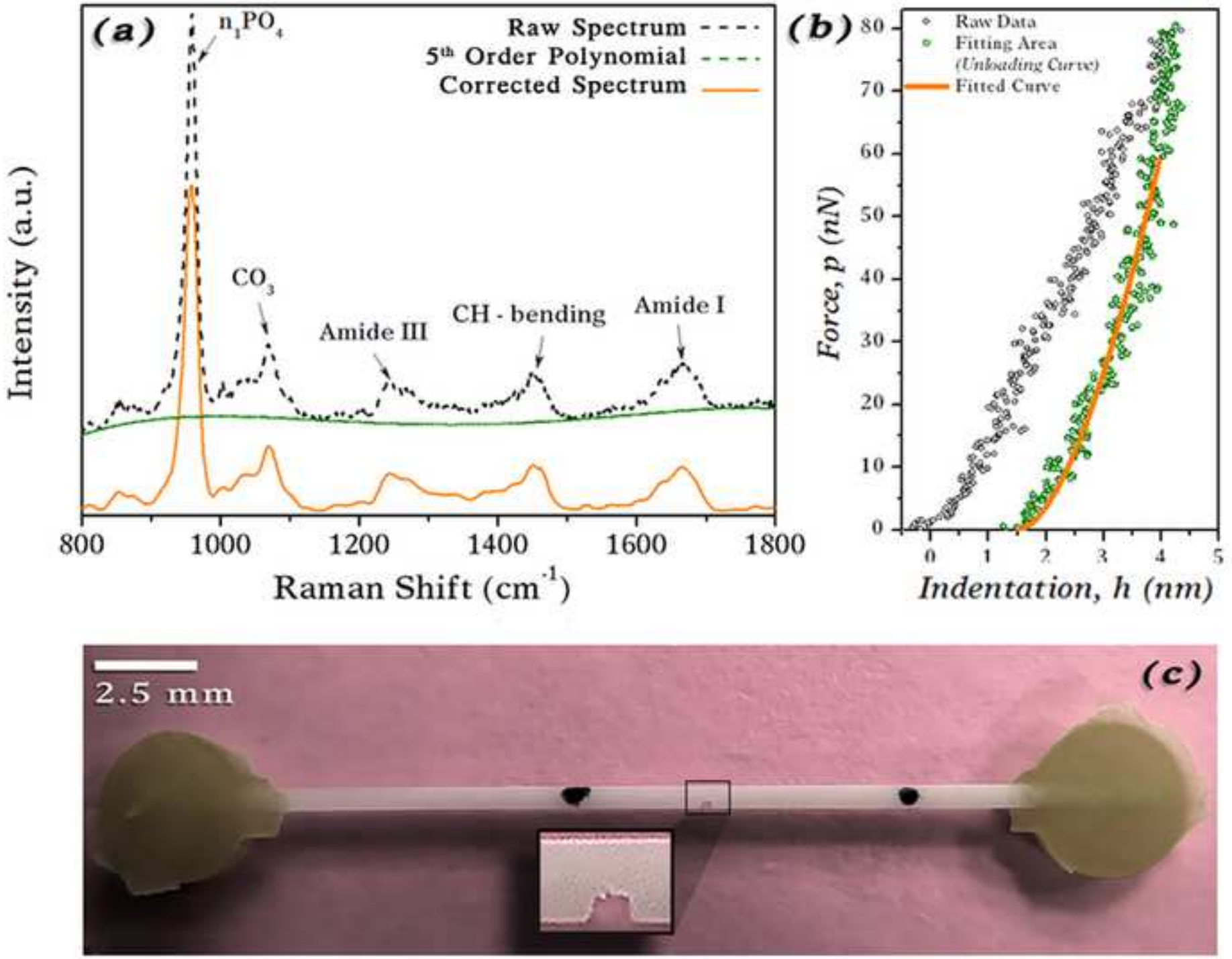

Figure 2

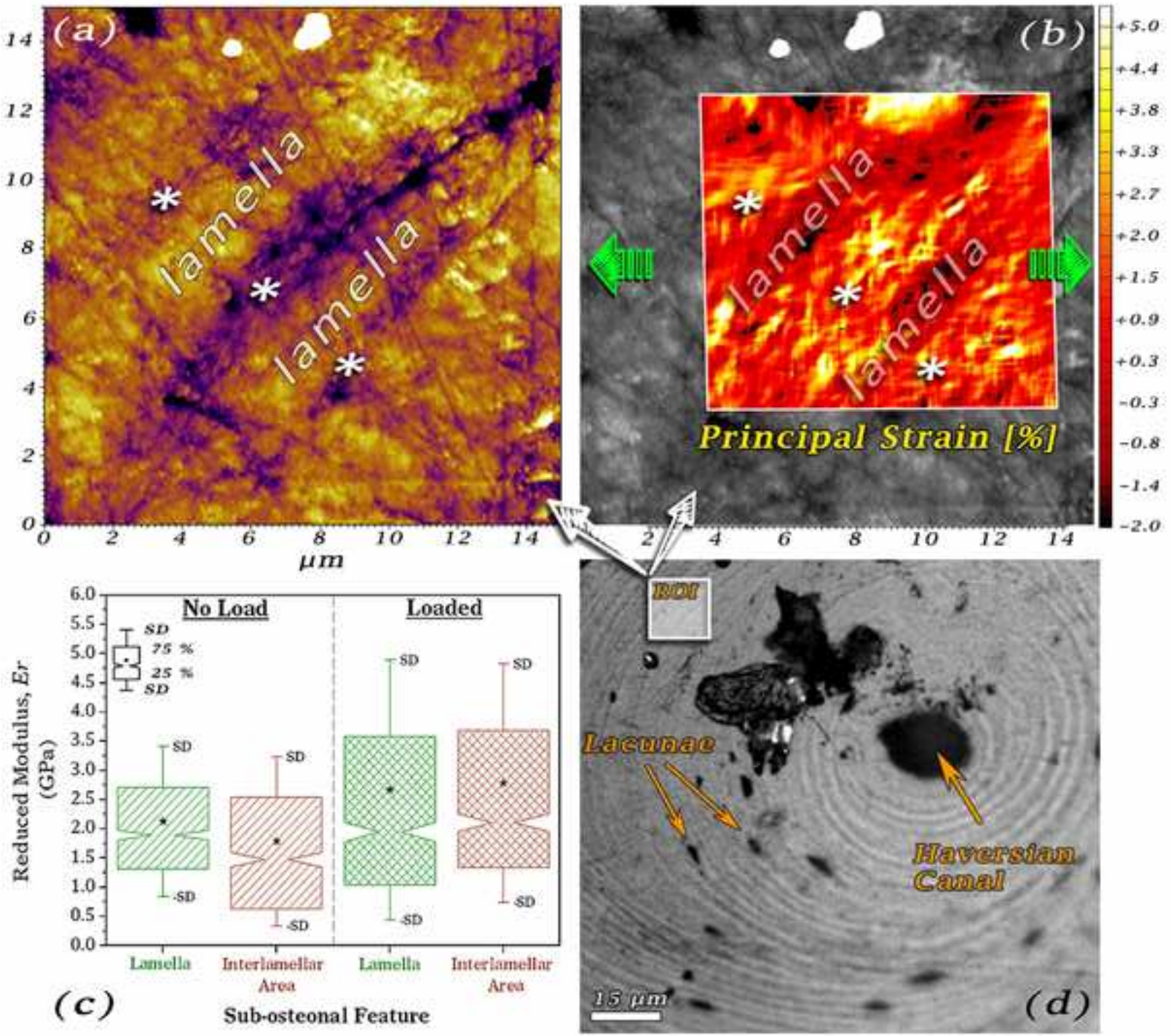

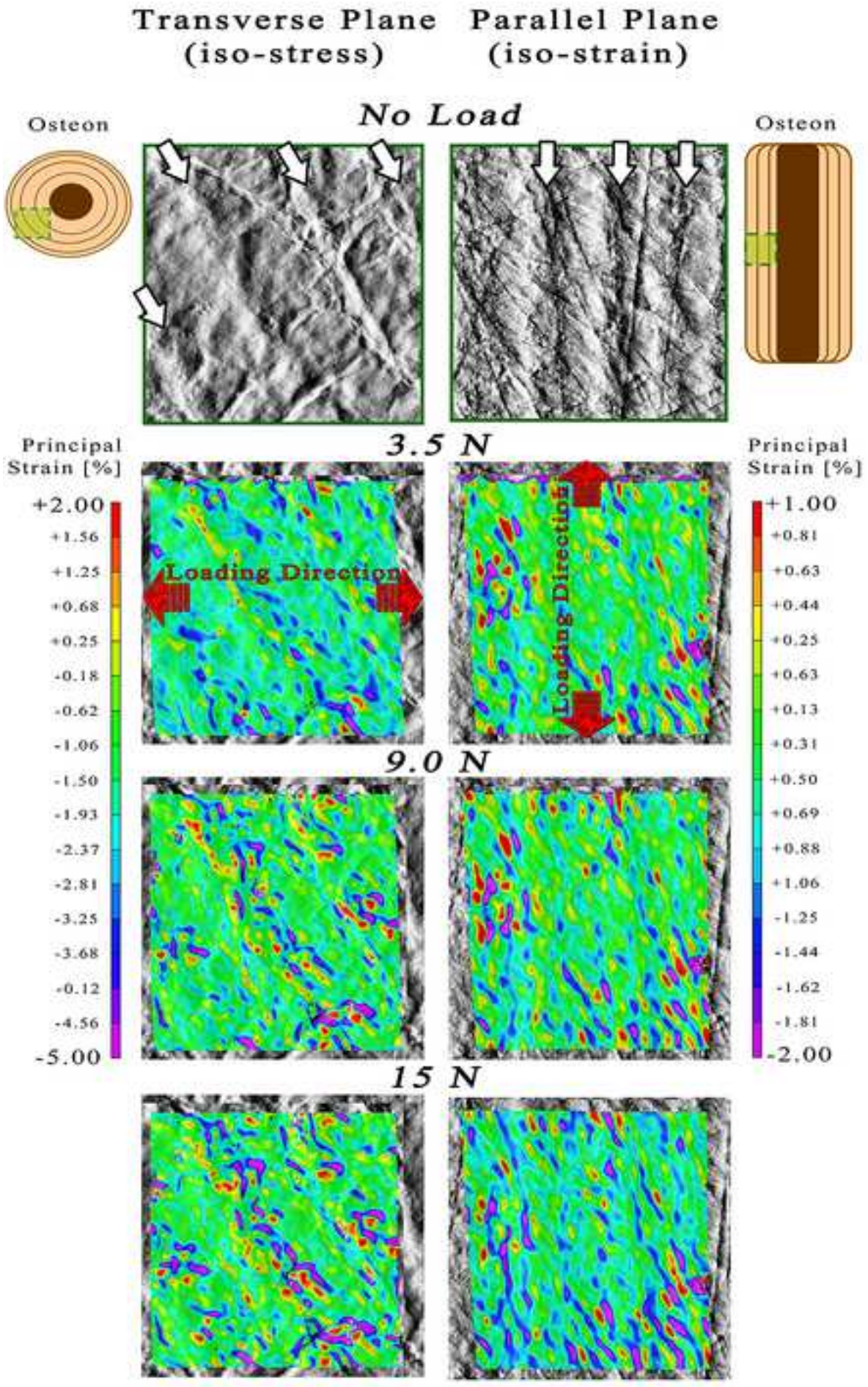

Figure 4

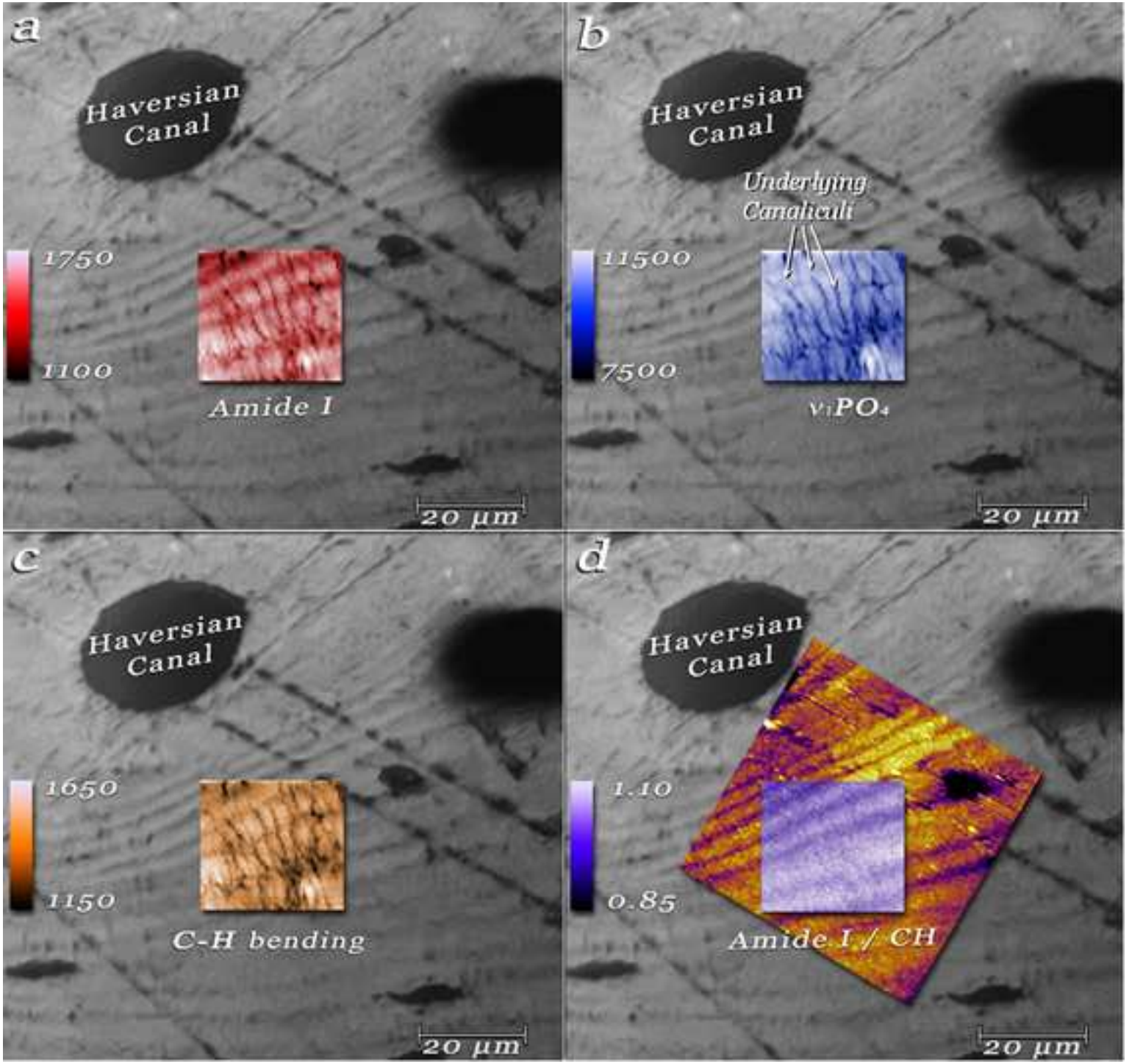

Figure 5

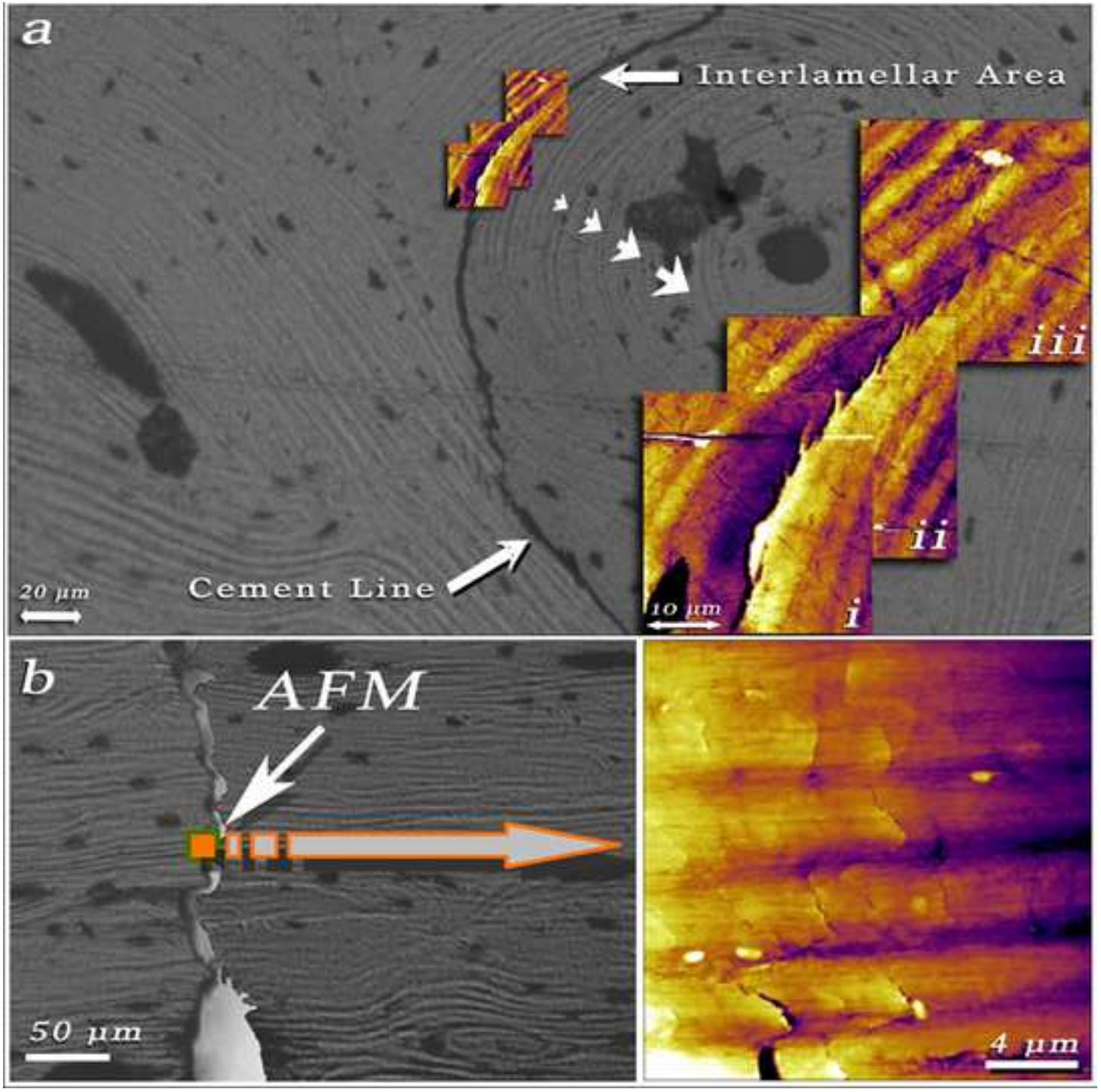

Figure 6

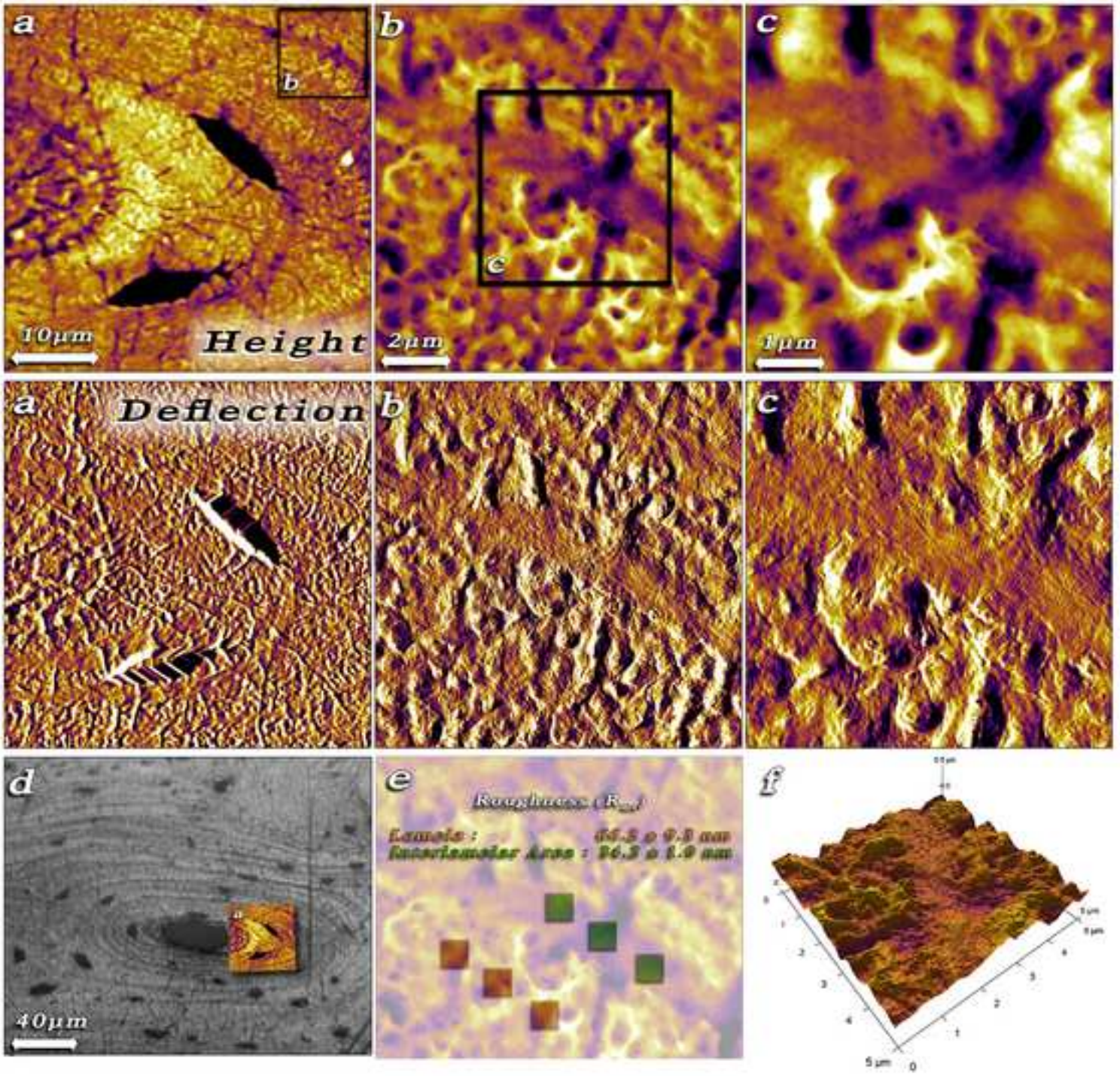

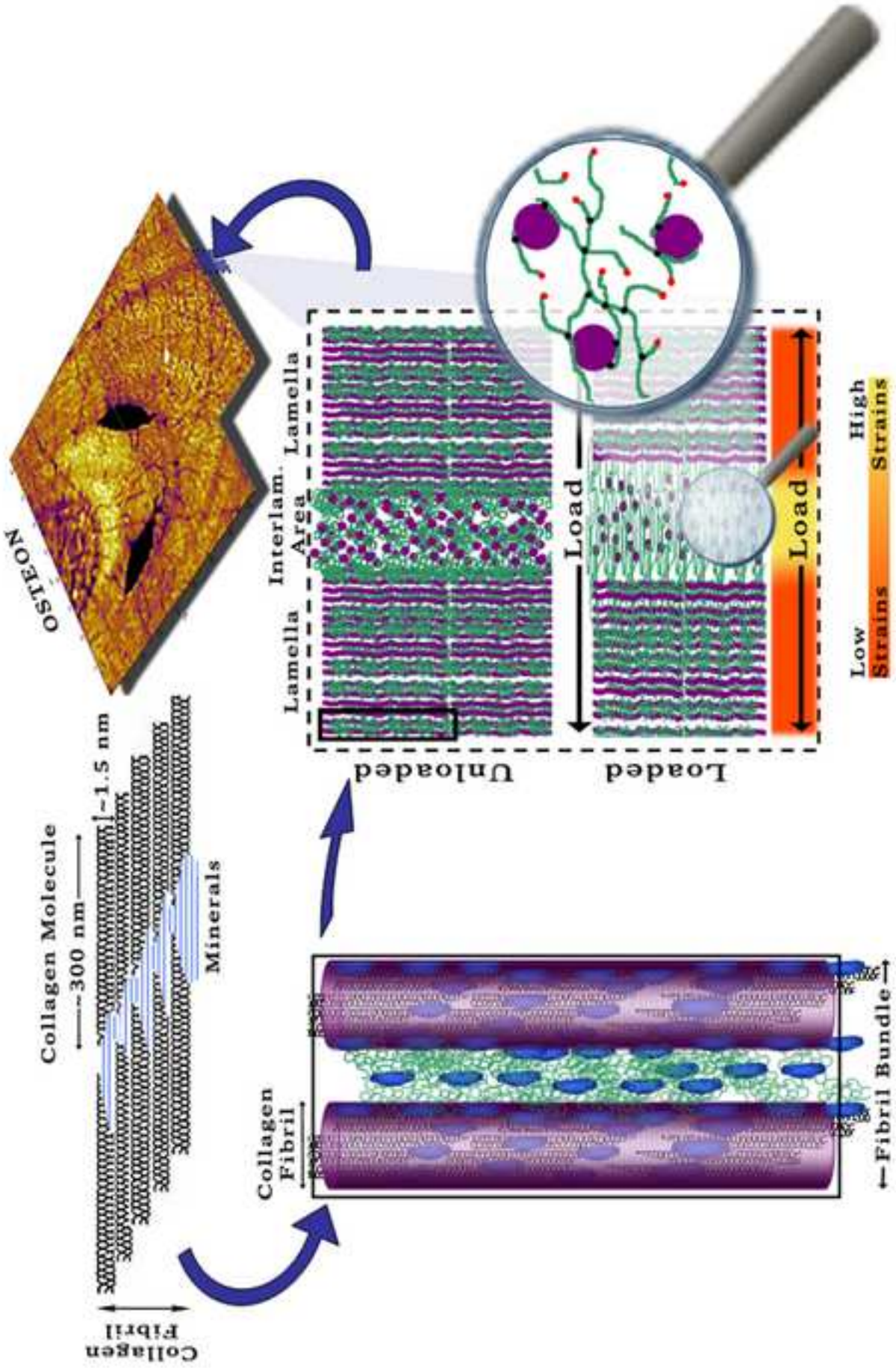
OSTEON
Interlam. Area
Lamella
Lamella
Load
Load
Unloaded
Loaded
Low Strains
High Strains
Collagen Molecule
~300 nm
~1.5 nm
Minerals
Collagen Fibril
Collagen Fibril
Fibril Bundle

Figure 7